conformational change upon adsorption is observed for Cu–TBPP on Ag(110) (Fig. 3d), where the single adsorption state is characterized by a dihedral angle of 30°.

From this analysis we conclude that the molecular conformation of Cu–TBPP is driven by the nature of the molecule–surface interaction. This conformational adaptation within the molecules occurs in addition to the general tendency for an adsorbate molecular lattice to rotate with respect to the substrate in order to minimize the inequivalent number of adsorption sites[18]. It also goes beyond the observation of a gauche conformation in molecular layers[19]. The saturated hydrocarbon group on the DBP substituents interacts with the surface by a weak chemisorption and permits molecular mobility[13]. Small deviations of the Cu–TBPP conformation ($\sim 90 \pm 10°$) result from modification of the weak chemisorption in response to the atomic corrugation and spacing. In contrast, larger conformational adaptations ($\sim 45°$ and more) are dominated by stronger π–metal interaction at close proximity (typically $\ll 0.5$ nm) of the delocalized electron system of the phenyl and the porphyrin components to the metal.

Conformational analysis of adsorbed molecules permits a semi-quantitative analysis of the adsorbate molecular interaction energy. The degree of rotation of the phenyl–porphyrin bonds balances the intramolecular steric hindrance with the molecule–surface interactions. The rotational barrier for one phenyl–porphyrin bond of tetra-aryl porphyrins in liquids has been measured by thermally activated isomerization of specific isomeric forms (isolated atropisomers) using NMR spectroscopy[20–22] and chromatography. Depending on the central metal atom, substituent and solvent, values of 80–140 kJ per mol per bond[20–22] have been published. This compares favourably with the 100 kJ per mol per bond resulting from a numerical simulation performed for a Cu–TBPP molecule in vacuum[17]. For the 30° dihedral angle observed for Cu–TBPP adsorbed on Ag(110), we estimate an energy of about 320 kJ per mol per bond. This conformation change is accompanied by an increased mixing of the π orbitals of the porphyrin and the phenyls, resulting in reconjugation of π orbitals throughout the molecule. As a result the lateral dimension of the TBP lobes in the STM data for Ag(110) (Fig. 3d) increases, whereas the contrast difference between substituent and centre of the porphyrin decreases to 0.3 nm (compare Cu(100) ~0.8 nm). For comparison, we attempted to perform scanning tunnelling spectroscopy experiments on various parts of the adsorbed porphyrins; but our current–voltage measurements resulted in decay of the molecules, precluding conventional analysis.

STM recognition of the orientation of molecular subunits should provide insights into the detailed geometric factors involved in adsorbent–adsorbate interactions. The conformational changes that we observe reflect the interaction strength of the molecule with the substrate and its geometry. □

Received 27 September 1996; accepted 24 February 1997.

1. Haran, A., Waldeck, D. H., Naaman, R., Moons, E. & Cahen, D. *Science* **263,** 948–950 (1994).
2. Burroughes, J. H. *et al. Nature* **347,** 539–541 (1990).
3. Sheats, J. R. *et al. Science* **273,** 884–888 (1996).
4. Salaneck, W. R. & Brédas, J. L. *Adv. Mater.* **8,** 48–52 (1996).
5. Chen, C. J. *Introduction to Scanning Tunneling Microscopy* (Oxford Univ. Press, New York, 1993).
6. Wiesendanger, R. *Scanning Probe Microscopy and Spectroscopy: Methods and Applications* (Cambridge Univ. Press,, 1994).
7. Seth, J. *et al. J. Am. Chem. Soc.* **116,** 10578–10592 (1994).
8. Bonnett, R. *Chem. Soc. Rev.* **24,** 19–33 (1995).
9. Harima, Y. *et al. Appl. Phys. Lett.* **69,** 1059–1061 (1996).
10. Song, H., Reed, C. A. & Scheidt, W. R. *J. Am. Chem. Soc.* **111,** 6865–6866 (1989).
11. Erler, B. S., Scholz, W. F., Lee, Y. J., Scheidt, W. R. & Reed, C. A. *J. Am. Chem. Soc.* **109,** 2644–2652 (1987).
12. Miyamoto, T. K., Sugita, N., Matsumoto, Y., Sasaki, Y. & Konno, M. *Chem. Lett.* 1695–1698 (1983).
13. Jung, T. A., Schlittler, R. R., Gimzewski, J. K., Tang, H. & Joachim, C. *Science* **271,** 181–184 (1996).
14. Sautet, P. & Joachim, C. *Chem. Phys. Lett.* **185,** 23–30 (1991).
15. Sautet, P. & Joachim, C. *Surf. Sci.* **271,** 387–394 (1992).
16. Chavy, C., Joachim, C. & Altibelli, A. *Chem. Phys. Lett.* **214,** 569–575 (1993).
17. Ercolessi, F., Parrinello, M. & Tosatti, E. *Phil. Mag. A* **58,** 213–226 (1988).
18. Modesti, S., Gimzewski, J. K., Schlittler, R. R. & Chavy, C. *Phys. Rev. Lett.* **72,** 1036–1039 (1994).
19. Rabe, J. P., Buchholz, S. & Askadskaya, L. *Synth. Met.* **54,** 339–349 (1993).
20. Eaton, S. S. & Eaton, G. R. *J. Am. Chem. Soc.* **97,** 3660–3666 (1975).
21. Crossley, M. J., Field, L. D., Forster, A. J., Harding, M. M. & Sternhell, S. *J. Am. Chem. Soc.* **109,** 341–348 (1987).
22. Dirks, J. W., Underwood, G., Matheson, J. C. & Gust, D. *J. Org. Chem.* **44,** 2551–2555 (1979).
23. Gottwald, L. K. & Ullman, E. F. *Tetrahedron Lett.* **36,** 3071–3074 (1969).
24. Hatono, K., Anzai, K., Nishino, A. & Fujii, K. *Bull. Chem. Soc. Jpn.* **58,** 3653–3654 (1985).

Acknowledgements. We thank C. Joachim, H. Tang, P. Guéret and H. Rohrer for enlightening discussions; E. Haskal and W. Riess for discussions and assistance; and K. I. Sugiura, T. Takami and Y. Sakata for synthesizing and providing the molecules. This work was supported in part by the Swiss Federal Office for Education and Science, through the ESPRIT basic research project 'Processing on the nanometer scale (PRONANO)'.

Correspondence and requests for materials should be addressed to T.A.J. (e-mail: thomas.jung@psi.com).

Increased plant growth in the northern high latitudes from 1981 to 1991

R. B. Myneni*, C. D. Keeling†, C. J. Tucker‡, G. Asrar§ & R. R. Nemani‖

* *Department of Geography, Boston University, Commonwealth Avenue, Boston, Massachusetts 02215, USA*

† *Scripps Institution of Oceanography, La Jolla, California 92093-0220, USA*

‡ *NASA Goddard Space Flight Center, Code 923, Greenbelt, Maryland 20771, USA*

§ *Office of Mission to Planet Earth, NASA Headquarters, Washington DC 20546, USA*

‖ *School of Forestry, University of Montana, Missoula, Montana 59812, USA*

Variations in the amplitude and timing of the seasonal cycle of atmospheric CO_2 have shown an association with surface air temperature consistent with the hypothesis that warmer temperatures have promoted increases in plant growth during summer[1] and/or plant respiration during winter[2] in the northern high latitudes. Here we present evidence from satellite data that the photosynthetic activity of terrestrial vegetation increased from 1981 to 1991 in a manner that is suggestive of an increase in plant growth associated with a lengthening of the active growing season. The regions exhibiting the greatest increase lie between 45° N and 70° N, where marked warming has occurred in the spring time[3] due to an early disappearance of snow[4]. The satellite data are concordant with an increase in the amplitude of the seasonal cycle of atmospheric carbon dioxide exceeding 20% since the early 1970s, and an advance of up to seven days in the timing of the drawdown of CO_2 in spring and early summer[1]. Thus, both the satellite data and the CO_2 record indicate that the global carbon cycle has responded to interannual fluctuations in surface air temperature which, although small at the global scale, are regionally highly significant.

We have made use of data from the advanced Very High Resolution Radiometers (AVHRRs) on board the National Oceanic and Atmospheric Administration (NOAA) series of meteorological satellites (NOAA-7, -9 and -11). From daily observations of channel 1 (wavelengths ~0.58–0.68 μm) and channel 2 (~0.72–1.1 μm) reflectances, global land data sets of normalized difference vegetation index (NDVI) were produced[5,6]. The NDVI is expressed on a scale from −1 to +1. It is between −0.2 and 0.05 for snow, inland water bodies, deserts and exposed soils, and increases from about 0.05 to 0.7 for progressively increasing amounts of green vegetation[7]. NDVI data are strongly correlated with the fraction of photosynthetically active radiation (wavelength 0.4–0.7 μm) absorbed by vegetation[8], that is, to the photosynthetic activity of vegetation canopies[9]. Two global data sets of NDVI were analysed: (1) the land segment of the joint NOAA/NASA Earth Observing System AVHRR Pathfinder data set at 8 km spatial resolution and 10-day intervals, for the period July 1981 until the end of June 1991[6], and (2) the Global Inventory Monitoring and Modelling Studies

(GIMMS) AVHRR NDVI data set at a similar spatial resolution, but at 15-day intervals, for the period January 1982 until the end of December 1990[10]. The Pathfinder data were calibrated to correct for post-launch degradation from estimates of the relative annual degradation rates (in %) of the two channels: 3.6 and 4.3 (NOAA-7), 5.9 and 3.5 (NOAA-9) and 1.2 and 2.0 (NOAA-11)[11]. NOAA-9 data were used for inter-satellite normalization. The GIMMS data were independently calibrated[12]; they are considered here to illustrate how a different calibrating scheme affects derived trends in the AVHRR data.

For each equal-area pixel and at either 10- or 15-day intervals, depending on which of the two satellite data sets was used, the maximum of NDVI with minimal atmospheric effects was retained[13]. The NDVI data from high northern latitudes (>40° N) did not show anomalies related to the El Chichon volcanic eruption during the mid-1982 to 1983 time period. These effects in the low latitude data were not corrected for in either of the two satellite data sets.

The calibrated Pathfinder NDVI data still showed residual non-vegetation-related variations[14]. We revised them by adjusting the NDVI for a hyper-arid portion of the Sahara desert (1.42×10^6 km^2) which has been found to be invariant as viewed by all three satellites[10]. An alternate correction scheme based on desert pixels from 10° N to 50° N yielded nearly identical results. Importantly, when this desert correction was applied to the NDVI anomaly time series of desert pixels from five-degree latitude bands between 10° N and 50° N, the residuals resembled noise.

Time series of spatially averaged monthly NDVI, evaluated as the mean of three 10-day maximum value NDVI composites, comprising a 10-year record, are plotted, first directly for reference (Fig. 1a), and then as anomalies to display interannual variability (Fig. 1b). Averaged for regions north of 45° N (uppermost curve in Fig. 1b) the NDVI anomaly shows evidence of increasing amplitude, summer values being low early in the record, high near the end. The NDVI anomaly in the tropics shows a large increase starting from November 1988, which also coincided with the change in satellites from NOAA-9 to NOAA-11. A somewhat smaller increase is seen during the switch from NOAA-7 to NOAA-9 in January 1985, although this increase began in the last months of the NOAA-7 record (and the anomaly north of 45° N actually shows a decrease). This raises a question regarding anomalous variations in NDVI from sensor changes. Although efforts have been made to establish

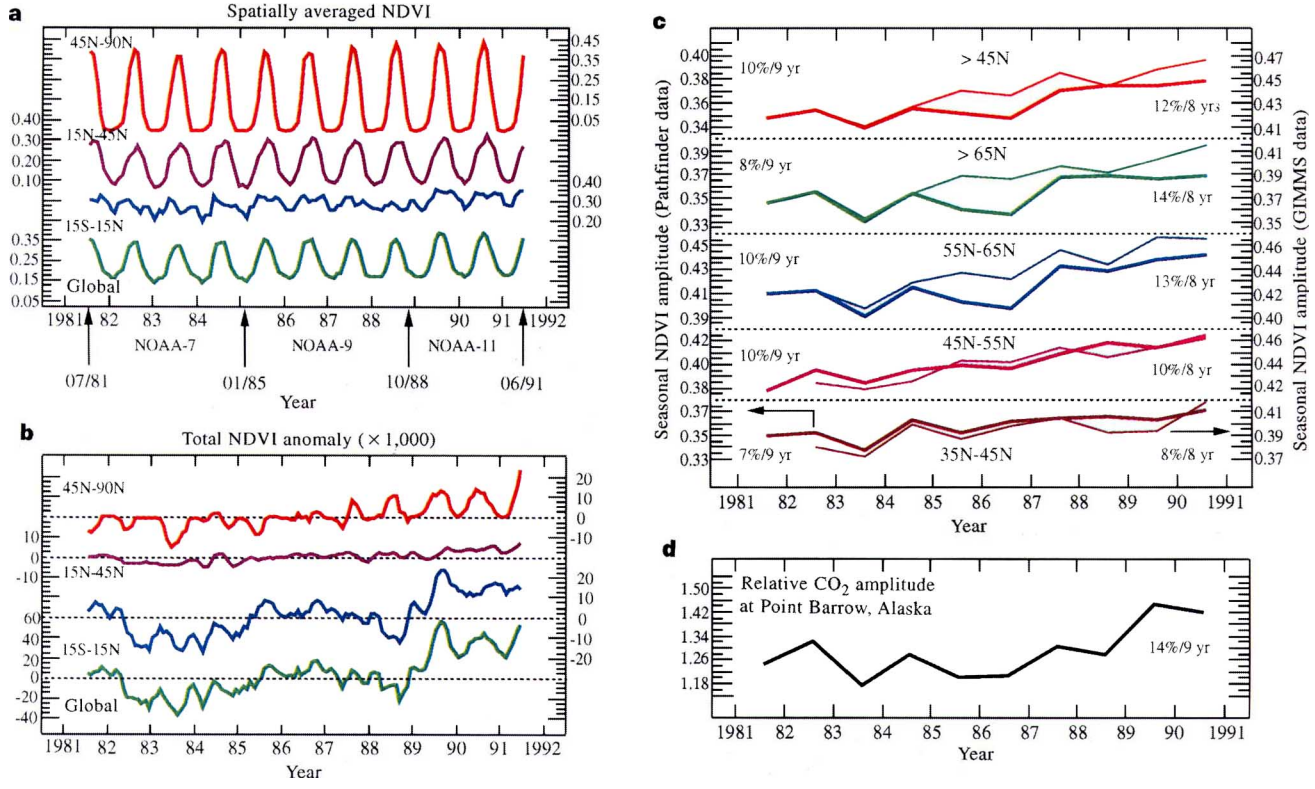

Figure 1 Time variations in normalized difference vegetation index (NDVI) compared with changes in amplitude of the seasonal cycle of atmospheric CO_2 for the period from July 1981 to the end of June 1991. The data in **a** and **b** have been smoothed by a 3-month running mean. Zonal total NDVI and its anomaly were calculated from pixels having a 10-year monthly average NDVI greater than 0.1 and within 3σ of the monthly average. The first condition guaranteed that bare or sparsely vegetated pixels were not included in spatial averages, while the second condition removed most of the influence of snow and bad scan-lines. **a**, Monthly average NDVI for selected latitudinal bands and the whole globe. The zonal total NDVI was normalized by the total vegetated land area in the month of August to obtain a zonal average that exhibited seasonality[14]. **b**, Monthly total anomalies of the above, expressed as departures from the 10-year record averages of monthly NDVI, summed over each latitudinal band[14] for each month. The vertical scale of the global plot is twice that of individual latitudinal bands. **c**, Seasonal amplitude of NDVI averaged over selected latitudinal bands. The amplitude, defined as the July and August average, is a good approximation because, at the northern latitudes shown, the winter-time NDVI value is close to zero. Spatial averaging was for July and August data combined over pixels with 10-year averages of NDVI greater than 0.1, in order to exclude bare areas, such as the great deserts of Asia. Results from both the Pathfinder (left ordinate) and GIMMS (right ordinate) NDVI data sets are shown together with the corresponding rates of increase. The higher rates of increase inferred from GIMMS data may be due to the lack of desert correction for the version of GIMMS data used in this analysis. **d**, Seasonal amplitude of atmospheric CO_2 relative to a base-period of 1961–67 as registered at Point Barrow, Alaska (71° N, 157° W)[1]. Linear trend estimates of the increase in seasonal amplitudes of NDVI and CO_2 are statistically significant (10% level) for all latitudinal bands shown. However, the limitations of regression analysis on short samples, that is, the determination of trend in the presence of low-frequency variations, must be noted.

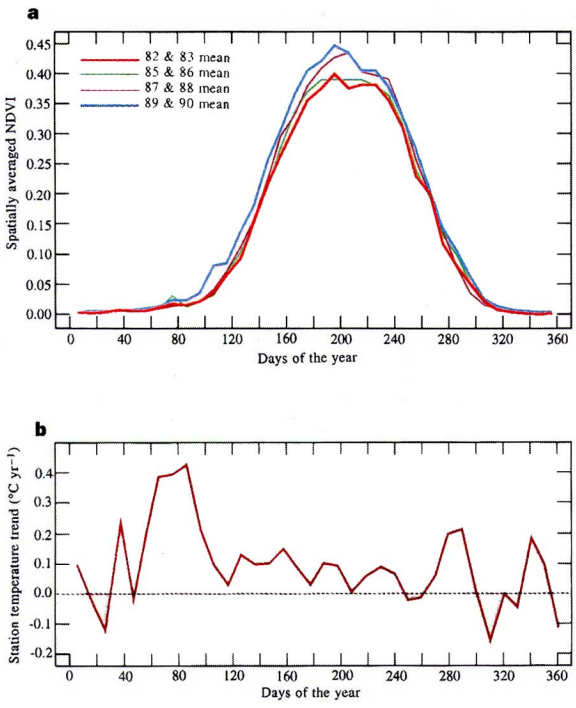

Figure 2 Interannual changes in seasonality of NDVI and in surface temperature, averaged north of 45° N, for selected pairs of years from 1982 to the end of 1900. **a**, NDVI averaged from 10-day maxima in NDVI for 1982–3, 1985–6, 1987–8 and 1989–90. Data from 1984 were not included because the number of years was odd. Spatial averaging was similar to that described in Fig. 1a legend. Changes in the timing of the active growing season over this 9-year record period were estimated from differences between the first and last bi-yearly average profiles at six threshold values of NDVI (from 0.1 to 0.35 in 0.05 increments). These values occurred during intervals of about 60 days each in spring and autumn when, respectively, NDVI was increasing and decreasing, at almost a constant rate. The six estimates each of the timing of rise and fall of NDVI may actually be correlated because of low-frequency variations (for example, soil moisture and/or equatorial sea surface temperature oscillations), and therefore, the standard errors given in the text must be interpreted in light of this limitation. We also inferred similar changes in the active growing season duration from an alternate pixel-by-pixel and year-by-year analysis[14]. **b**, Changes in the annual cycle of near-surface air temperature from 1982 to 1990. Daily thermometer observations of maximum and minimum temperature were averaged in order to approximate daily mean temperatures and interpolated on a 1 × 1 degree grid[22]. The daily data were further averaged over three separate approximately 10-day periods per month to obtain 36 observations per year. These 10-day average temperatures were then linearly regressed on the year (from 1982 to the end of 1990) to obtain the slopes shown here.

proper inter-sensor calibration linkages[11,12], some residual effects cannot be ruled out, especially between NOAA-9 and NOAA-11[14]. This situation, for example, confounds proper interpretation of the tropical NDVI anomaly time series. For instance, intense sea surface temperature (SST) oscillatory events in the tropical Pacific and Atlantic oceans from 1982 to early 1989 have been linked to decreased vegetation growth in large regions of the semi-arid tropics[15]. The increase in tropical and global NDVI anomaly starting from late 1988 also coincided with an unprecedented decline in atmospheric CO_2 anomaly, from a peak value in late 1988 to a minimum in late 1993[16]. Nevertheless, these interpretations, as they involve the NDVI data, are limited by possible sensor change effects.

Changes in the amplitude of the seasonal cycle of NDVI at northerly latitudes greater than 35° N are plotted in Fig. 1c, as characterized by changes in the July and August average NDVI. This broad measure of the seasonal maximum approximates the seasonal amplitude because winter-time NDVI at these northern latitudes is close to zero (compare Fig. 1a). The seasonal amplitude, by this definition, increased by 7 to 14%, depending on the latitude and data set, from 1981 or 1982 to the end of 1990 (Fig. 1c). Because NDVI is a measure of photosynthetic activity of vegetation as noted above[8,9], this increase indicates a substantial change in photosynthetic activity of plants at higher northern latitudes. A similar increase (14%) is indicated in the amplitude of the seasonal cycle of atmospheric CO_2 measured at Point Barrow, Alaska[1] (Fig. 1d). This CO_2 cycle, although observed in the Arctic (71° N), registers changes in CO_2 gas exchanges, and hence in the biotic activity of plants and soil over all northern temperate and polar latitudes[17]. Together, the NDVI and CO_2 data indicate increased biospheric activity north of about 35° N. Two recent studies have also reported increased photosynthetic activity in the northern high latitudes as increased biomass from deposition in European forests[18] and from tree-ring analysis in Mongolia[19], respectively.

Timing of the seasonal rise and fall in NDVI suggests possible changes in the length of the active growing season, that is, the period during which photosynthesis actually occurs (as opposed to the concept of growing season, measured for example in degree days. As shown in Fig. 2a in Pathfinder data, the rise in NDVI, spatially averaged from 45° N to the northern limit of the data, came progressively earlier in the season between 1982 and 1990, as shown by successive 10-day averages, where each plot shows an average over two years for clarity. Because spatially averaged NDVI rose each year at nearly a constant rate from early April (about day 110) to late June (about day 170) the advance in the active growing season is apparent, notwithstanding the relatively coarse time resolution (10 day) afforded by the NDVI data. From six estimates of the time advance at six successive thresholds of NDVI, we estimate an advance of 8 ± 3 days (Fig. 2a).

An advance of about 7 days in the seasonal cycle was previously inferred from atmospheric CO_2 data as having taken place between the 1960s and early 1990s, with most of the increase occurring after 1980 (Fig. 1 of ref. 1). The NDVI data suggest that this increase occurred over an extensive region of the extratropical Northern Hemisphere. The NDVI data in Fig. 2a further indicate a prolongation of the declining phase of the active growing season, estimated at 4 ± 2 days between 1982–3 and 1989–90. Therefore, the active growing season north of 45° N appears to have lengthened by 12 ± 4 days over the 1980s. These estimates must be interpreted as suggestive of a longer active growing season, rather than in an absolute sense, in view of the coarse temporal resolution (10 days) and residual atmospheric effects in NDVI data. The associated standard errors given here are not rigorous, for low-frequency variations in NDVI data invalidate the assumption of statistical independence required of the successive threshold values.

Variations in the amplitude and timing of the seasonal cycle of atmospheric CO_2 have shown an association with surface air temperature consistent with the hypothesis that warmer temperatures have promoted increases in biospheric activity outside the tropics[1,2]. A likely cause is an increase in the length of the active growing season brought about by warmer temperatures[1]. As shown in Fig. 2b, a pronounced increase in late-winter and early-spring temperatures took place over the period of NDVI changes, especially during March.

Because of their high spatial resolution (relative to ground-based meteorological measurements), NDVI data provide spatial detail of where the average changes in amplitude and timing of the active growing season occurred. To address regional variations in NDVI, we show in Fig. 3 a map related to the time plots shown in Fig. 1 together with a map of the 9-year average of NDVI for comparison.

The linear rate of change in NDVI, averaged over the 9 years of

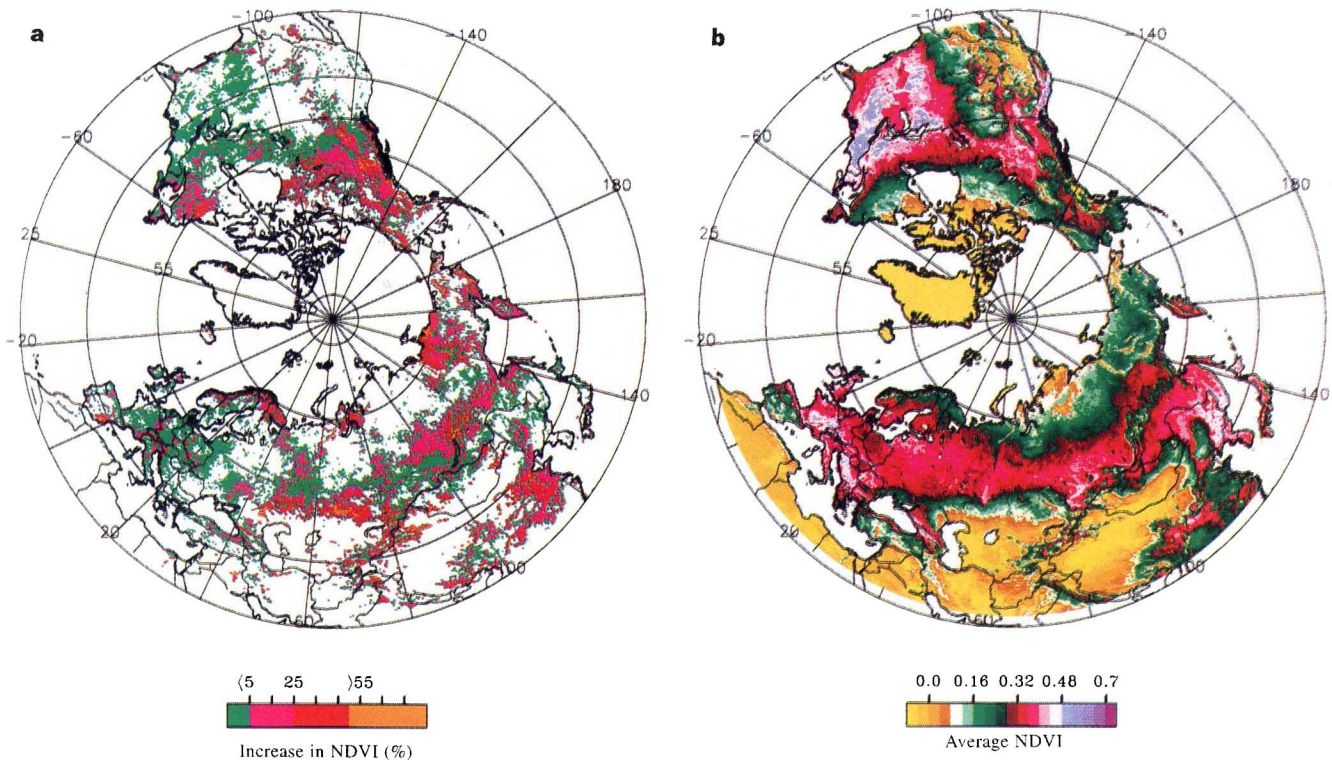

Figure 3 Geographical distribution of the change from 1982 to 1990 in NDVI of land areas north of 27.75° N, expressed as the average over the northern active growing season of May to the end of September. **a**, NDVI increase in percentage over 9 years, determined by linear regression of year-to-year northern growing season averaged NDVI, aggregated to 0.25 × 0.25 degree pixels from original 8-km-resolution data. Only estimates with a positive slope and a statistically significant (10% level) regression coefficient were contoured. There were no pixels with statistically significant negative slopes. Again, we emphasize the limitations of regression analysis on short-term samples. **b**, Nine-year average NDVI over northern active growing season of May to the end of September determined by averaging the monthly NDVI of 0.25 × 0.25 degree pixels from 1982 to 1990.

seasonal NDVI data in northern latitudes, from 1982 to the end of 1990, are mapped in Fig. 3a. Data were averaged from May to the end of September, to approximate the main active growing season of land vegetation in the Northern Hemisphere.

In Eurasia, a band of increasing NDVI extends from Spain in a northeasterly direction across Asia to the western Pacific Ocean. In this band, central Europe, southern Russia, and a broad region near Lake Baikal in Siberia are most affected. Outside this band, northern Scandinavia, northern China, and northeastern Siberia are also strongly affected. In North America, a band of increasing NDVI extends from Alaska in a southeasterly direction to the Great Lakes, thence northeasterly to Labrador. In this band, northwestern Canada is most strongly affected. Outside this band, the continental United States (excluding Alaska) and the area around the Hudson Bay show little change in NDVI.

In general, the regions of greatest increase in NDVI are inland from the oceans, except in the Arctic, and are north of 50° N. The prominent bands of increased NDVI referred to above in both Eurasia and North America, correspond generally to areas of high NDVI (Fig. 3b). Thus most of the areas where changes in NDVI amplitude and seasonality were observed are also regions of significant vegetation density. Notable exceptions are several Arctic regions in Eurasia where NDVI rose sharply from low initial values.

We believe the increasing trend in photosynthetic activity of the northern high latitudes, inferred from satellite observations of NDVI amplitude and phase, to be robust despite varying satellite overpass times and the lack of an explicit atmospheric correction. These effects, however, could modify the magnitudes of NDVI amplitude and estimates of the active growing season duration.

Analyses of station temperature trends during 1961–90 indicate pronounced warming over substantial areas in Alaska, northwestern Canada and northern Eurasia[3]. The greatest warming, up to 4 °C, has occurred in winter. Only slightly less warming has occurred in the same regions in spring, but considerably less warming in summer and even less in autumn[3]. Associated with warming at high latitudes is an approximate 10% reduction in annual snow cover from 1973 to the end of 1992, especially an earlier disappearance of snow in spring (Table 1 of ref. 4). Where snow-lines have retreated earlier due to enhanced warming, we expect an early start of the active growing season.

The winter and spring warming in the interior of the continents of Asia and North America in the 1980s may be a result of natural causes not yet explained, but its timing is consistent with an enhanced greenhouse effect caused by build-up of infrared-absorbing gases in the atmosphere[20]. The unusual warming which peaked near 1990 was of global extent. Although it amounted to a departure of only a few tenths of a degree from previous record temperatures[21], it was associated with far greater warming in the spring months at high northern latitudes. Biospheric activity there, based on our analysis, increased remarkably as a result of this warming, suggesting that small changes in global temperature may reflect disproportionate responses at the regional level, and may be accompanied by positive feedbacks which can markedly influence processes such as photosynthesis and litter decomposition. □

Received 29 August 1996; accepted 3 March 1997.

1. Keeling, C. D., Chin, J. F. S. & Whorf, T. P. Increased activity of northern vegetation inferred from atmospheric CO_2 measurements. *Nature* **382,** 146–149 (1996).
2. Chapin, F. S., Zimov, S. A., Shaver, G. R. & Hobbie, S. E. CO_2 fluctuation at high latitudes. *Nature* **383,** 585–586 (1996).
3. Chapman, W. L. & Walsh, J. E. Recent variations of sea ice and air temperatures in high latitudes. *Bull. Am. Meteorol. Soc.* **74,** 33–47 (1993).

4. Groisman, P. Ya, Karl, T. R. & Knight, T. W. Observed impact of snow cover on the heat balance and the rise of continental spring temperatures. *Science* **263,** 198–200 (1994).
5. Tucker, C. J. in *Advances in the Use of NOAA AVHRR Data for Land Applications* (ed. D'Souza, D.) 1–19 (European Economic Union Press, Brussells, 1995).
6. James, M. E. & Kalluri, S. N. V. The Pathfinder AVHRR land data set: an improved coarse-resolution data set for terrestrial monitoring. *Int. J. Remote Sens.* **15,** 3347–3364 (1994).
7. Tucker, C. J., Fung, I. Y., Keeling, C. D. & Gammon, R. H. Relationship between atmospheric CO_2 variations and a satellite-derived vegetation index. *Nature* **319,** 195–199 (1986).
8. Asrar, G., Fuchs, M., Kanemasu, E. T. & Hatfield, J. L. Estimating absorbed photosynthetic radiation and leaf area index from spectral reflectance in wheat. *Agron. J.* **76,** 300–306 (1984).
9. Myneni, R. B., Hall, F. G., Sellers, P. J. & Marshak, A. L. the interpretation of spectral vegetation indexes. *IEEE Trans. Geosci. Remote Sens.* **33,** 481–486 (1995).
10. Tucker, C. J., Newcomb, W. W. & Dregne, A. E. AVHRR data sets for determination of desert spatial extent. *Int. J. Remote Sens.* **15,** 3547–3566 (1994).
11. Rao, C. R. N. & Chen, J. Inter-satellite calibration linkages for the visible and near-infrared channels of the advanced Very High Resolution Radiometer on the NOAA-7, -9, and -11 spacecraft. *Int. J. Remote Sens.* **16,** 1931–1942 (1995).
12. Los, S. O. Calibration adjustment of the NOAA AVHR Normalized Difference Vegetation Index without recourse to component channel 1 and 2 data. *Int. J. Remote Sens.* **14,** 1907–1917 (1993).
13. Holben, B. N. Characteristics of maximum value composite images for temporal AVHRR data. *Int. J. Remote Sens.* **7,** 1417–1437 (1986).
14. Myneni, R. B., Tucker, C. J., Asrar, G., Keeling, C. D. & Nemani, R. R. Increased vegetation greenness amplitude and growing season duration in northern high latitudes inferred from satellite-sensed vegetation index data from 1981–91. *NASA Tech. Memo. 104638* (NASA Goddard Space Flight Center, Greenbelt, MD, 1996).
15. Myneni, R. B., Los, S. & Tucker, C. J. Satellite-based identification of linked vegetation index and sea surface temperature anomaly areas from 1982–1990 for Africa, Australia and South America. *Geophys. Res. Lett.* **23,** 729–732 (1996).
16. Keeling, C. D., Whorf, T. P., Wahlen, M. & van der Plicht, J. Interannual extremes in the rate of rise of atmospheric carbon dioxide since 1980. *Nature* **375,** 666–670 (1995).
17. Heimann, M., Keeling, C. D. & Tucker, C. J. in *Aspects of Climate Variability in the Pacific and Western Americas* (ed. Peterson, D. H.) 277–303 (Geophys. Monog. Ser., Am. Geophys. Union, Washington DC, 1989).
18. Kauppi, P. E., Mielikainen, K. & Kuusela, K. Biomass and carbon budget of European forests from 1971–1990. *Science* **256,** 70–74 (1992).
19. Jacoby, G. C., D'Arrigo, R. D. & Davaajamts, T. Mongolian tree rings and 20th-century warming. *Science* **273,** 771–773 (1996).
20. Houghton, J. T. *et al.* (eds) *Climate Change 1995* 1–365 (Cambridge Univ. Press, 1995).
21. Jones, P. D., Wigley, T. M. L. & Briffa, K. R. in *Trends '93: A Compendium of Data on Global Change* (eds Boden, T. A., Kaiser, D. P., Sepanski, R. J. & Stoss, F. W.) (ORNL/CDIAC-65, Oak Ridge, TN, 1994).
22. Piper, S. C. & Stewart, E. F. A gridded global data set of daily temperature and precipitation for terrestrial biosphere modelling. *Glob. Biogeochem. Cycles* **10,** 757–782 (1996).

Acknowledgements. We thank S. C. Piper and E. F. Stewart for analysis of the station temperature data, S. C. Piper and T. P. Whorf for discussions, and S. Los for help in the calibration of GIMMS NDVI data. This work was supported by the Office of Mission ot Planet Earth of NASA. E. F. Stewart's collaboration was made possible by funds from the Electric Power Research Institute and the USNSF.

Correspondence should be addressed to R.B.M. (e-mail: rmyneni@crsa.bu.edu).

Large-scale tectonic deformation inferred from small earthquakes

Falk Amelung* & Geoffrey King

Institut de Physique du Globe, 5, Rue Rene Descartes, F-67084 Strasbourg, France

It is a long-standing question whether the focal mechanisms of small earthquakes can be used to provide information about tectonic deformation on a regional scale. Here we address this question by using a 28-year record of seismicity in the San Francisco Bay area to compare the strain released by small earthquakes with geological, geodetic and plate-tectonic measurements of deformation in this region. We show that on a small spatial scale, the strain released by small earthquakes is closely related to specific geological features. But when averaged over a regional scale, strain release more closely follows the regional pattern of tectonic deformation: this relationship holds for all but the largest earthquakes, indicating that the earthquake strain is self-similar[1,2] over a broad range of earthquake magnitudes. The lack of self-similarity observed for the largest earthquakes suggests that the time interval studied is not large enough to sample a complete set of events—the fault with the highest probability[3] for hosting one such missing event is the Hayward fault.

* Present addresses: Department of Geophysics, Stanford University, Stanford, California 94305, USA (F.A.); Institut de Physique du Globe, Laboratoire de Tectonique, Tour 24, BP89, 4 Place Jussieu, 75252 Paris, France (G.K.).

Following the formulation by Kostrov[4], the seismic strain of a block in the Earth's crust can be obtained from the geometric moment tensors

$$\epsilon_{ij} = \frac{1}{2V}\sum_{n=1}^{N} \mathcal{M}_{ij}^{(n)} \qquad (1)$$

where $\mathcal{M}_{ij}^{(n)}$ is the geometric moment tensor of the nth earthquake, N is the number of earthquakes and V is the volume of the block. The geometric moment tensor of an earthquake is given by $\mathcal{M}_{ij} = \int_A u \mathrm{d}A(u_i n_j + u_j n_i)$, where A is the surface of the fault, dA is a surface element, u is the slip in the earthquake, and u_i and n_i are the unit slip and fault-normal vectors, respectively. The geometric moment tensor $\mathcal{M}_{ij}$, referred to by Ben-Menahem and Singh[5] as "potency", is related to the seismic moment tensor M_{ij} used in seismology by $M_{ij} = \mu\mathcal{M}_{ij}$ (ref. 6), where μ is the shear modulus.

The strain in a local region, $\epsilon_{ij}^{(\mathrm{loc})}$, is related to the strain in a larger region, $\epsilon_{ij}^{(\mathrm{reg})}$, by a fourth-order tensor that is a complicated function of time and space. Here we consider special cases in which they are assumed to be linearly related by

$$\epsilon_{ij}^{(\mathrm{loc})} = c\epsilon_{ij}^{(\mathrm{reg})} \qquad (2)$$

where c is the amplitude of the local deformation, that is, the shape and the orientation of the local and regional strain tensors are identical but their amplitudes can be different. For homogeneous deformation, $c = 1$. If seismic strain is self-similar and if $\epsilon_{ij}^{(\mathrm{loc})}$ is the seismic strain by earthquakes in one scale, then equation (2) will apply at any scale with different values for c. Some examples are

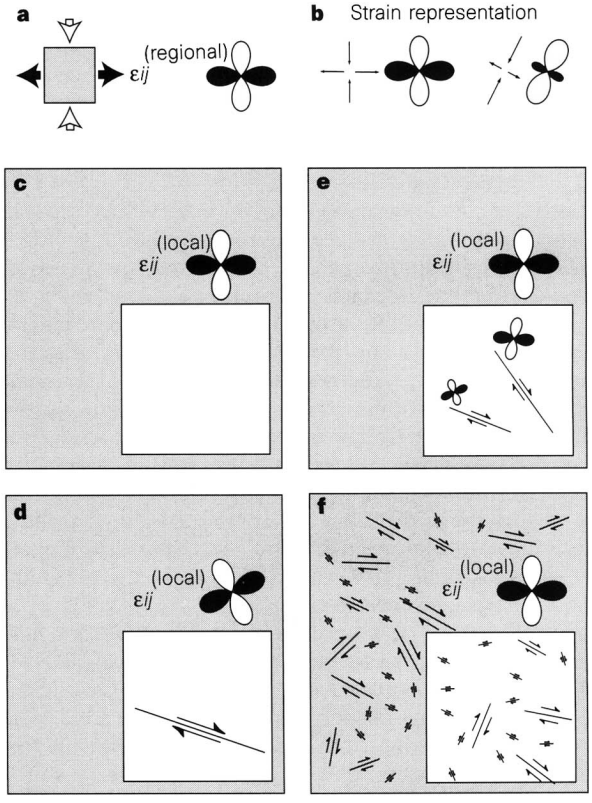

Figure 1 Homogeneous and inhomogeneous deformation in four different regions subject to pure shear. **a**, Boundary conditions and imposed strain. **b**, The strain tensor is represented by two-dimensional strain rosettes for the horizontal components. White lobes indicate directions of contraction, black lobes indicate directions of extensions. **c**, Homogeneous deformation. **d**, Inhomogeneous deformation due to an individual shear fault. **e**, Inhomogeneous deformation due to two faults. **f**, Quasi-homogeneous deformation due to many shear faults with a variety of orientations.